Phase discontinuity classification from single-aperture irradiance patterns using machine learning

Thomas E. DeFoor[a], Timothy J. Bukowski[a], Matthew Kalensky[b], and Stanislav Gordeyev[a]

[a]University of Notre Dame, South Bend, Indiana, United States
[b]Naval Surface Warfare Center Dahlgren Division, Dahlgren, Virginia, United States

ABSTRACT

This paper explores the efficacy of employing machine learning, specifically an encoder-style convolutional neural network, to estimate the magnitude of an optical-phase discontinuity ($|\Delta\phi|$) that results in an aberrated, far-field irradiance pattern. The model receives a single 32×32 normalized irradiance pattern image and returns the estimated $|\Delta\phi|$. We train and validate the model using simulated data with varying values of $\Delta\phi$ (from 0 to 2π radians), discontinuity locations within the aperture of the simulated system, and strengths of background noise. In exploring this trade space, we calculate the mean absolute errors of the model to be between 0.0603 and 0.475 radians. We also explore the model's versatility using varying spot sizes to augment the transfer of this model across various systems where the focal length, aperture diameter, or light wavelength may differ, thereby influencing the number of pixels holding information across each irradiance pattern. Finally, this model is tested on experimentally collected data using a spatial light modulator, resulting in a mean absolute error of 0.909 radians. This research supports the development of a shock-wave-tolerant phase reconstruction algorithm for the Shack–Hartmann wavefront sensor. At large, robust shock-wave-tolerant phase reconstruction algorithms will improve wavefront sensing efforts where shock waves are present.

Keywords: Aero-Optics, Machine Learning, Shock Waves, Wavefront Sensing

1. INTRODUCTION

It is of current interest to implement laser propagation systems onto aircraft. A hemispherical turret is the most common beam director geometry for this specific application. An example optical turret is shown in Fig. 1. Unfortunately, the turret is not an aerodynamic body and impedes the flow. This gives rise to a turbulence environment that imposes phase aberrations onto an outgoing or incoming laser beam.[1–6] Furthermore, at flight speeds near, at, or above the speed of sound, the local flow will accelerate to sonic over the surface of the turret. When this occurs, a shock wave will form resulting in a near-discontinuous change in gas properties. For example, we see an increase in freestream density across the shock wave resulting in a change in the local index of refraction, n, of the air.[7,8] This change in refractive index is related to a change in optical-path length. The spatial mean removed optical-path length, otherwise known as optical-path difference, OPD, can be related to optical phase, ϕ, through the relation, $\Delta\phi = (-2\pi/\lambda) * \Delta OPD$. Accordingly, the aberrations caused by shock waves can result in decreased performance for laser propagation systems.

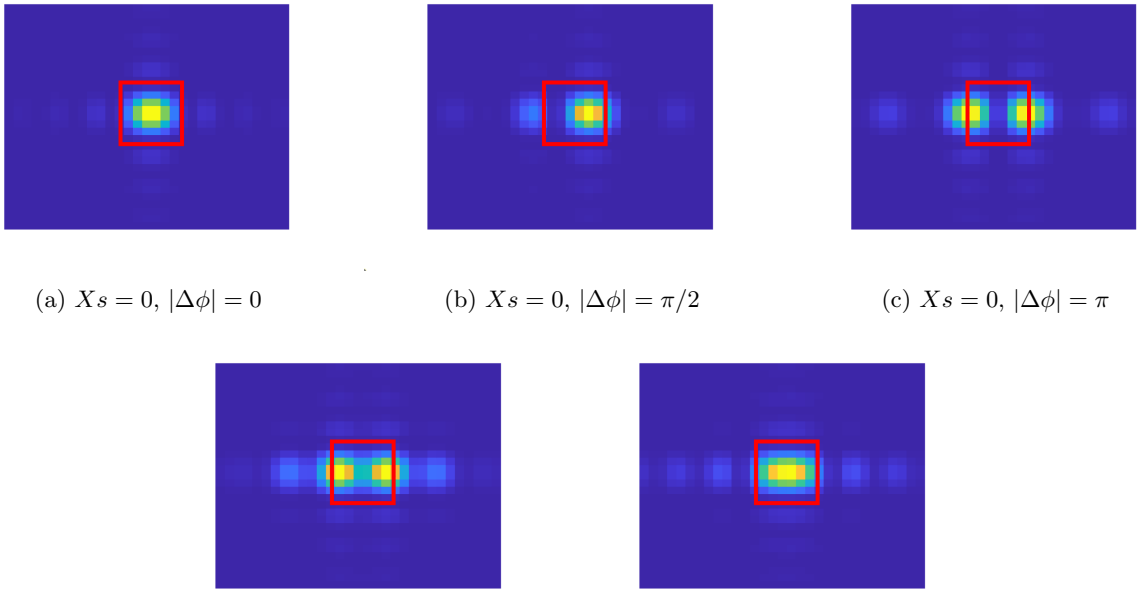
Previous studies into the effects of shock waves on propagating beams have shown that this shock wave-induced $\Delta\phi$ leads to appreciable beam spreading and a bifurcation of the far-field, irradiance pattern.[9–12] It has been shown that the degree of bifurcation is related to the strength of the shock wave. For this paper, we model the shock wave as a phase discontinuity. The simulated images in Fig. 2 show varying degrees of irradiance pattern bifurcation caused by varying the magnitude and location, Xs, of a phase discontinuity within the pupil of an aperture. Here Xs is defined as a fraction of the aperture diameter, D, away from the center. Traditionally, a Shack–Hartmann Wavefront Sensor (SHWFS) is used in conjunction with a least-squares reconstruction algorithm to estimate the OPD field. This sensor uses an array of sub-aperture lenslets to focus portions of the incoming OPD onto a detector screen. When a phase tilt is present across the lenslets, the

Further author information: (Send correspondence to Thomas E. DeFoor)
Thomas E. DeFoor: E-mail: tdefoor@nd.edu

Unconventional Imaging, Sensing, and Adaptive Optics 2024, edited by Jean J. Dolne, Santasri R. Bose-Pillai, Matthew Kalensky, Proc. of SPIE Vol. 13149, 131490F
© 2024 SPIE · 0277-786X · doi: 10.1117/12.3028274



Figure 1: Optical turret installed on University of Notre Dame's Airborne Aero-Optics Laboratory (AAOL). Image is from Ref. 7.



(a) $Xs = 0$, $|\Delta\phi| = 0$ (b) $Xs = 0$, $|\Delta\phi| = \pi/2$ (c) $Xs = 0$, $|\Delta\phi| = \pi$

(d) $Xs = 0.25$, $|\Delta\phi| = \pi$ (e) $Xs = 0.40$, $|\Delta\phi| = \pi$

Figure 2: Simulated far-field irradiance patterns disturbed by varying degrees of $|\Delta\phi|$ and locations within the aperture axes.

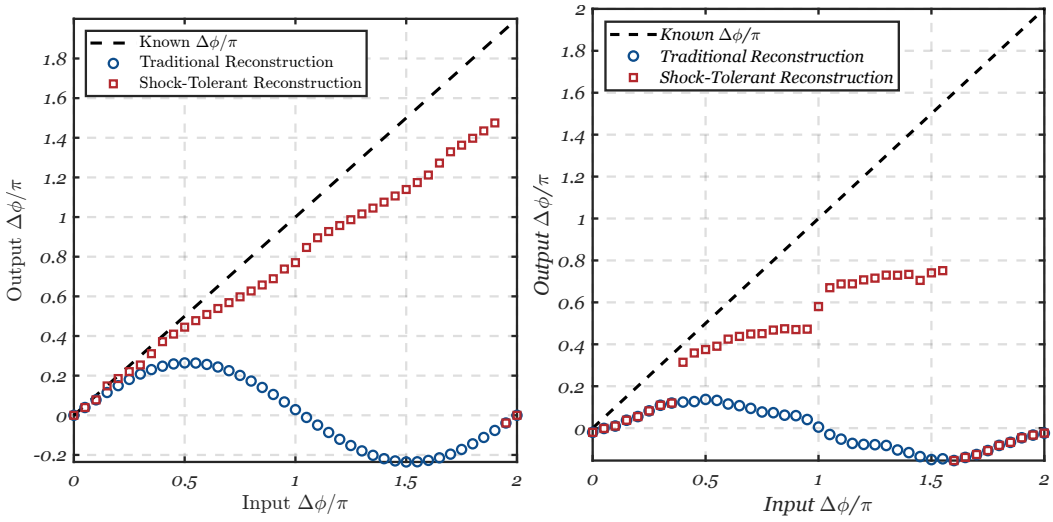
irradiance patterns will deviate from their on-axis locations. Using the measured irradiance pattern deviations as well as the focal length of the lenslets, we can estimate the phase tilts across the lenslets. These tilts are then used in a least-squares reconstruction algorithm to obtain a spatially continuous estimate of the incident OPD.[13–16]

It has been shown that least-squares OPD reconstruction from SHWFS data where a phase discontinuity, like those imposed by shock waves, is present across the measurement aperture fails to give accurate estimations when the magnitude of the phase discontinuity, $|\Delta\phi|$, is greater than 0.5π radians.[9] Past $|\Delta\phi| = 0.5\pi$ rad, the measured sub-aperture irradiance pattern shifts do not map proportionally to the tilted phase present in

the pupil plane, leading to inaccurate estimations of the OPD. One approach to creating a shock-wave tolerant phase reconstruction algorithm was developed in Ref. 17 which uses special weighting functions in the least squares reconstruction to exclude outlier points at the shock. A different preliminary shock-wave tolerant phase reconstruction algorithm has been developed and validated using both simulated and experimentally collected SHWFS imagery in the presence of an optical phase discontinuity as a first step to model the aberrations imposed by shock waves.[18] However, this approach relies on a heuristically driven relationship between the phase discontinuity and the ratio of the magnitude of the 1st and 2nd bifurcated peaks in the observation-plane irradiance pattern. Furthermore, this approach quickly loses effectiveness in cases when the discontinuity is offset from the center of the aperture, like those shown in Figs. 2d and 2e.

Despite the limitations of the current shock-wave-tolerant algorithm for the SHWFS, under some conditions, it drastically improved the estimated OPD over traditional reconstruction when a phase discontinuity was present. Figure 3 displays results from the current shock tolerant phase reconstruction algorithm for both simulated (left) and experimental (right) sets of optical phase discontinuity data. Plotted on the x-axis is the input $|\Delta\phi|$ inducing the far-field bifurcation and on the y-axis is the $|\Delta\phi|$ that is calculated from the reconstructed OPD field. The black dashed line in both plots represents the desired, one-to-one ratio between input and output. It can be seen that the shock tolerant method (plotted in red squares) shows improved performance relative to the traditional reconstruction method (plotted in blue circles). The results of this algorithm show that if accurate estimations of the $|\Delta\phi|$ are acquired, then least-squares reconstruction of the incident OPD will be more accurate.

In recent years, deep learning has become increasingly integrated into SHWFS data processing, demonstrating success in various stages. Applications range from finding centroid displacements,[19] to reconstructing the wavefront from a slope field,[20] to directly mapping the SHWFS irradiance pattern to the wavefront.[21,22] Machine learning has also been used for wavefront sensor fusion and wavefront prediction in aero-optics.[23–25] The purpose of this paper is to propose a robust solution to estimating the $|\Delta\phi|$ from the observation-plane irradiance patterns alone through the use of machine learning. In what follows, an encoder-style convolutional neural network (CNN) is developed to receive a single-aperture irradiance pattern image and return an estimated $|\Delta\phi|$. The model description and architecture are outlined in Sec. 2. After training, the model is then tested on various sets of simulated SHWFS data as well as experimentally collected data, the results of which are presented in Sec. 3. Section 4 then summarizes and concludes the paper.



(a) Simulated Data (b) Experimentally Collected Data

Figure 3: Reconstructed $\Delta\phi/\pi$ compared to input $\Delta\phi/\pi$ for the traditional and shock tolerant reconstruction algorithms. Both images are from Ref. 18.

2. MODEL

A CNN has been proposed for identifying phase discontinuities from observation-plane irradiance patterns due to its proven resilience in complex pattern recognition inside images.[26] Furthermore, CNNs house fewer trainable parameters and thus are less complex than traditional artificial neural networks, allowing for greater focus on the features trained in the model architecture.

In practice, CNNs will receive an input, usually an image, which is passed over by a kernel that filters patterns and features present in the input data, i.e., the convolution layer of the model. The outputs of the convolutional layers are passed through activation functions, which allow for improved recognition of higher-order or non-linear features in the data. The implementation of multiple convolutional layers in combination with non-linear activation functions allows for stratified pattern recognition where simpler features recognized in early layers are mapped to higher-order features in later layers.[26–29] These identified features are represented in a feature map which is sent to a pooling layer that further reduces the complexity and downsizes the data, extracting the most important information. Finally, the downsized data is flattened into a one-dimensional array so that it can be passed to a traditional, fully connected neural network that performs the necessary calculations to receive the estimated output.

For this study, the Keras 3 library was used in tandem with Tensorflow as the backend to seamlessly construct, train, and test our neural network models. The model used for this application is an encoder-style, regression CNN. Here, the first layer is a $32\times32\times1$ input layer representing the far-field irradiance pattern image, normalized by the maximum valued pixel in the image. This data is then sent to 3 convolution layers, each with a 3×3 kernel and the rectified linear unit function (ReLu) as the activation function, to ensure the outputs will always be positive, the reason for which is explained in Sec. 3.[27] These convolution layers are each separated by 2×2, max-pooling layers. Finally, the resulting feature map is flattened and sent to a fully connected neural network with 128 nodes and ReLu activation with one output, the estimated $\Delta\phi$. The specific model houses 158465 trainable parameters using the *adam* optimizer, allowing for the model to learn faster and more accurately.[30] The model is programmed to use mean absolute error as the loss function, which is monitored during training to minimize over-fitting using Keras' callbacks API with a patience of 5. Figure 4 shows a visual description of the model architecture. This model architecture was the result of multiple optimization trials and was chosen for its loss reduction and simplicity, resulting in fast and accurate estimations of $\Delta\phi$. It should be noted that this model architecture remains unchanged between the various instances of training and testing presented in Sec. 3.

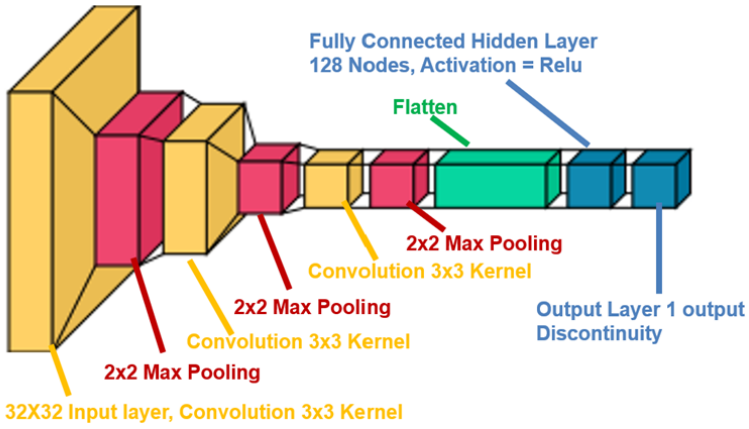


Figure 4: CNN Model architecture.

3. RESULTS

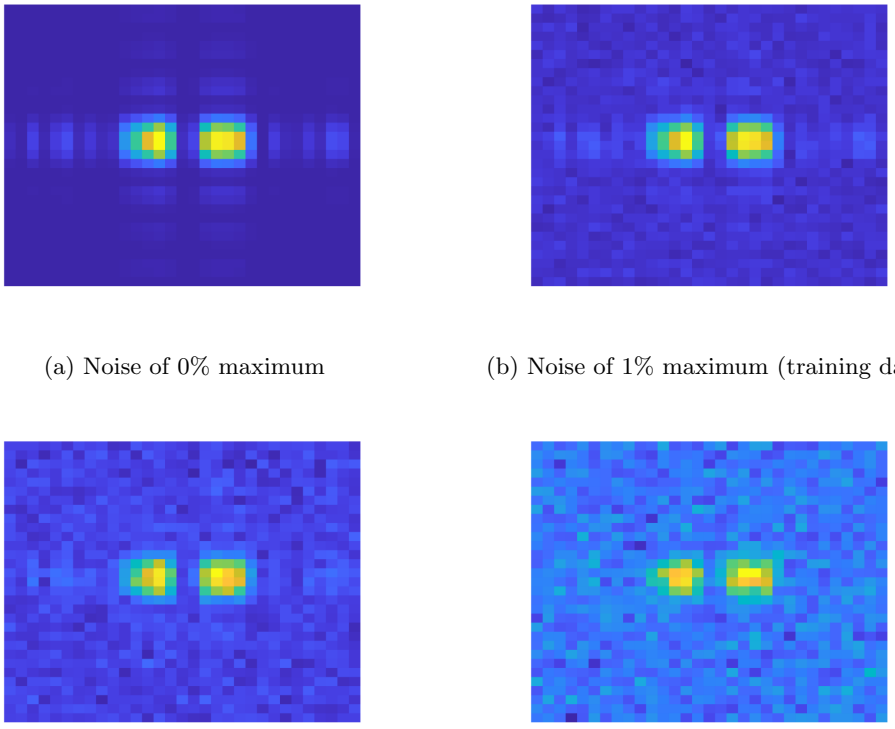
This section outlines the training and testing of the model described in Sec. 2. The model is first trained and validated using simulated irradiance imagery. Next, this model is tested for its versatility by examining its

accuracy with different irradiance pattern spot sizes. Finally, the model is tested on experimentally collected optical-phase discontinuity data.

3.1 SIMULATED RESULTS

Model training and testing were conducted to quantify how well the model outlined in Sec. 2 can recognize the associated shock-like $|\Delta\phi|$ behind the guise of varying discontinuity locations and degree of additive background noise. As shown in Fig. 2, the degree of bifurcation for an aperture-centered discontinuity is related to its strength. However, when this discontinuity approaches the edge of the aperture, the bifurcation pattern specific to that $|\Delta\phi|$ is hidden, in the case of Figs. 2d and 2e.

A set of simulated, single aperture, far-field irradiance pattern images was generated for varying shock strengths, modeled by a $|\Delta\phi|$ phase mask from 0 to 2π radians, and locations, Xs, from 0.00 to 0.40. It has been shown in Refs. 9, 18 that the bifurcation patterns are mirrored on either side of integer multiples of $\pm\pi$ and their placement is related to flow characteristics for which the current shock-tolerant algorithm can discern. Therefore, $|\Delta\phi|$ values were generated to 2π radians, and hence the use of the ReLu activation functions in the model architecture. The generation of these images follows the procedure outlined in Ref. 31. To maintain simplicity, it was assumed that the aperture was fully illuminated by unit-amplitude, collimated light, to which a thin-lens transmittance function was applied and angular-spectrum propagation was used to obtain the irradiance patterns shown in Fig. 2. This procedure was repeated four times with varying degrees of background noise. Noise levels were chosen to mimic the camera background noise in the experimental SHWFS data, which were estimated to be normally distributed values between 1% and 2% of the maximum irradiance value. Accordingly, data was generated with normally distributed additive noise of 0%, 1%, 2%, and 5% maximum (Fig. 5).



(a) Noise of 0% maximum

(b) Noise of 1% maximum (training data)

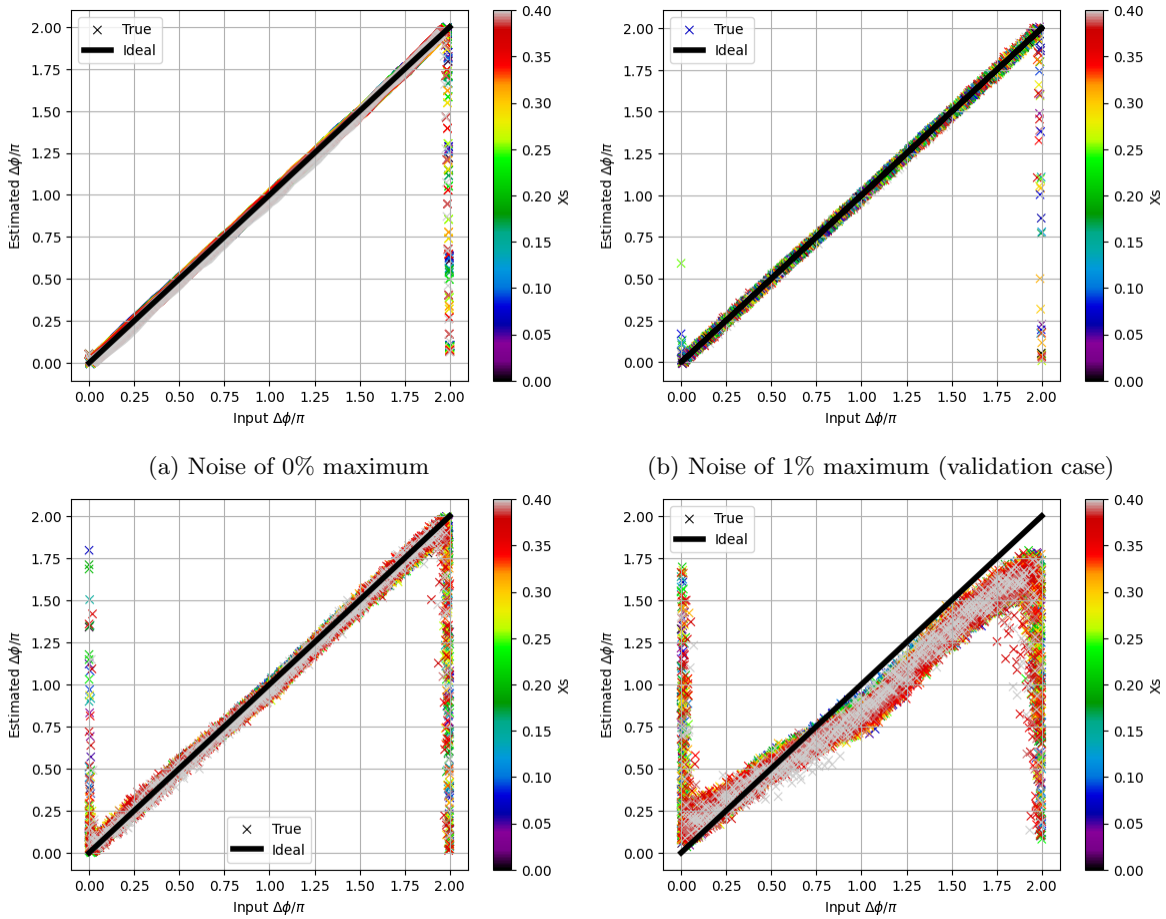
(c) Noise of 2% maximum

(d) Noise of 5% maximum

Figure 5: Simulated sample single aperture irradiance patterns with associated $|\Delta\phi|$ of π in varying degrees of additive background noise.

The training data for the model consisted of 25789, 32×32, grayscale irradiance images generated from the method outlined above in 1% noise. These training images were generated with simulated $\Delta\phi$ from 0 to 2π radians in increments of 0.01 radians and Xs from 0.00 to 0.40 (0% to 40% of the aperture diameter away from the center) in increments of 0.01. The model was trained on a randomized 80% set of the training data using monitored training to minimize the overall loss from the model. The model was then validated using the remaining unseen 20% of the training images, resulting in a mean absolute error of 0.052 radians.

Next, the model was tested on the full, randomized set of 25789 irradiance images for 0%, 2%, and 5% data. Testing resulted in mean absolute errors of 0.063 radians, 0.101 radians, and 0.475 radians, respectively. Figure 6 shows the result from the validation and test cases. This plot is similar to Fig. 3 where the x-axis is the input $\Delta\phi/\pi$, the y-axis is the output, a black line representing the desired relationship, with the addition of the shock location, Xs, represented by different colors, However, it should be noted that the results plotted are not values taken after OPD reconstruction but rather estimated phase step values taken directly from the model. As mentioned earlier, results from Ref. 18 show that OPD reconstruction is noticeably improved when accurate estimations of $|\Delta\phi|$ are obtained, therefore, no OPD reconstruction is performed in the present study.



(a) Noise of 0% maximum

(b) Noise of 1% maximum (validation case)

(c) Noise of 2% maximum

(d) Noise of 5% maximum

Figure 6: Input $\Delta\phi/\pi$ vs Model Returned $\Delta\phi/\pi$ for varying degrees of background noise.

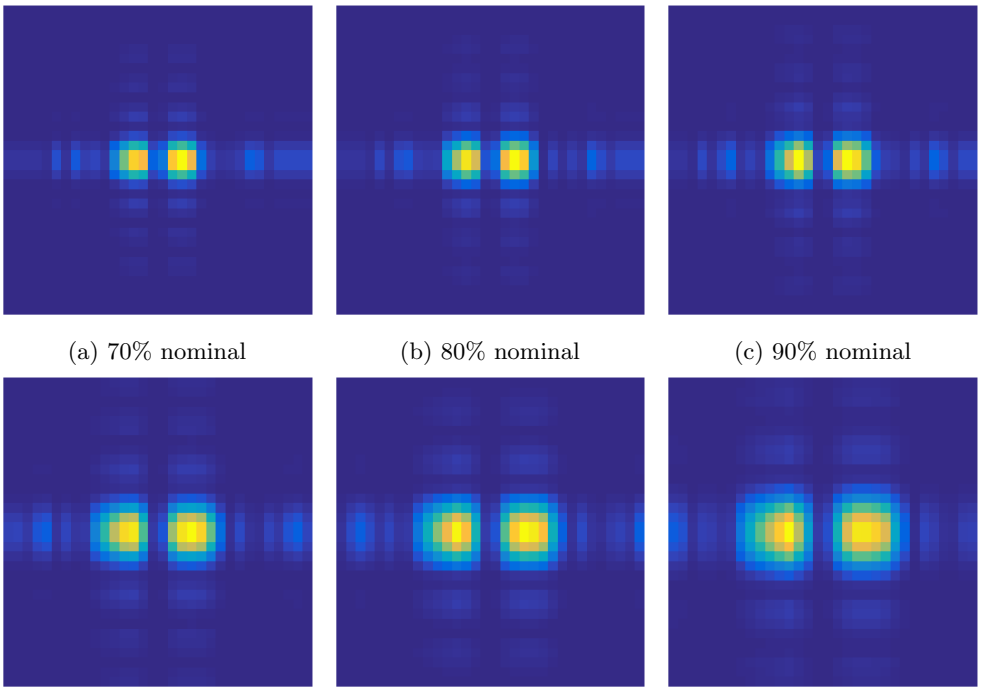
Figure 6 agrees with the expected result that the fully-trained CNN model is resistant to varying noise levels. Furthermore, the model proves to understand the necessary information about the features within the irradiance patterns in order to distinguish between different values of Xs. In the *extreme*, 5% noise case, the desired 1:1 trend between input and output $|\Delta\phi/\pi|$ is not fully attained, but the estimations from the model are still quite accurate. However, at discontinuities close to 0 and 2π radians, the model appears to estimate random

discontinuity values unrelated to the offset in the discontinuity location. This is especially seen in the 5% noise case, where the break-off from the expected occurs within 0.25π of 0 and 2π. This is believed to be a result of the model's inability to distinguish the small differences in irradiance patterns around the unperturbed cases of 0 and 2π radians. However, this does not pose a problem as at these discontinuities, any resulting distortion in the beam is negligible, so the usual centroiding algorithm could be used to correctly measure tilt. Therefore, it can be said with confidence that the model accurately estimates $\Delta\phi$ from irradiance patterns alone.

3.1.1 VERSATILITY

This section explores the versatility of the model tested and trained in Sec. 3.1. As the idea is to create one model able to be used across various systems, it is important to understand how the model will perform with varying simulated irradiance pattern sizes. Different SHWFS will have different characteristics, i.e., number of pixels available per sub-aperture. Different SHWFS systems may also have different lenslet focal lengths (f) and sub-aperture diameters (d) in addition to different wavelengths (λ) of propagating light. The differences in these parameters lead to varying spot sizes in the far-field since, for square apertures, the spot size goes as $\Delta X, \Delta Y \approx \lambda f/d$.[32]

To test the versatility of the model, the 0% noise imagery was resized using the built-in Keras image pre-processing layers. This data was slightly modified to only include $Xs = 0.0, 0.1, 0.2, 0.3$, and 0.4. The images were resized to 70%, 80%, 90%, 110%, 120%, and 130% their original size using bi-linear interpolation. Figure 7 shows the various image sizes.



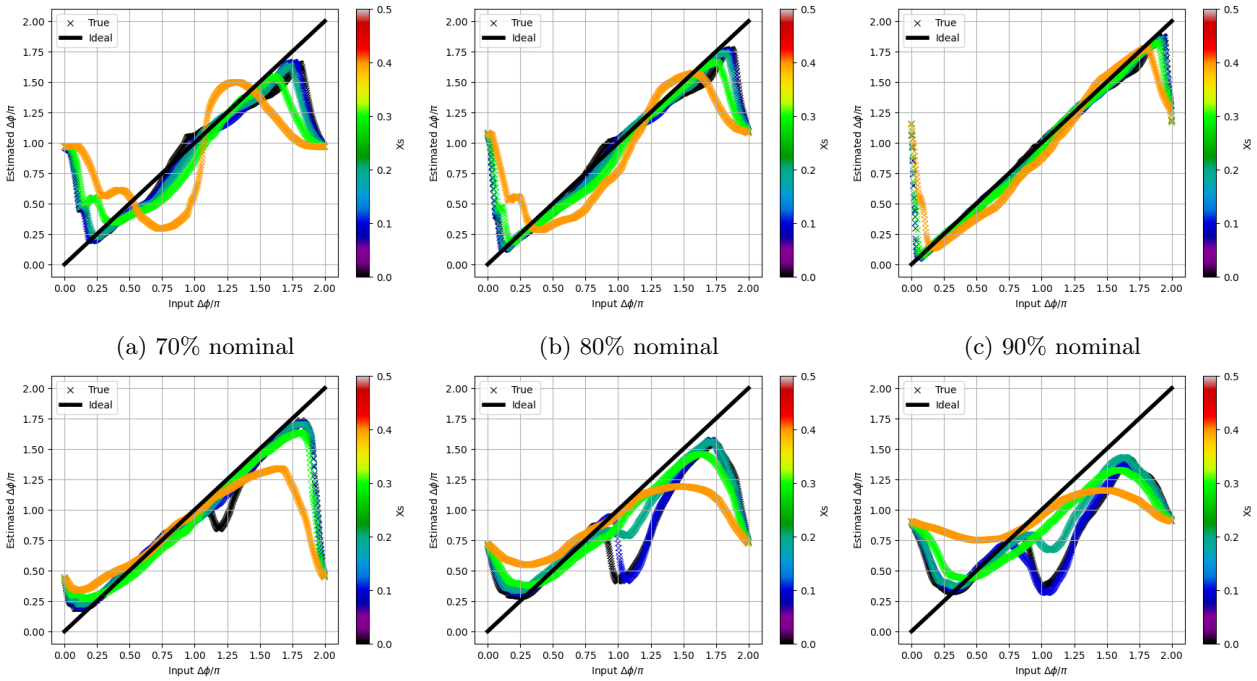
(a) 70% nominal (b) 80% nominal (c) 90% nominal

(d) 110% nominal (e) 120% nominal (f) 130% nominal

Figure 7: Simulated far-field irradiance patterns of varying spot sizes.

Testing the very same model on this set of data resulted in mean absolute errors of 1.064, 0.790, 0.481, 0.242, 0.494, and 0.789 radians for 70%, 80%, 90%, 110%, 120%, and 130%, respectively. The plots of estimated versus true phase jump can be found in Fig. 8 (the range of Xs on the plots was increased to 0.5 for visibility). In the case of smaller spot sizes, the model performs well with small error towards 0 and 2π radians for all Xs. For smaller spot sizes, the model performs well with slightly more error towards 0 and 2π radians. There is an exception with the 70% nominal case at $Xs = 0.4$, where the estimations from the model veer away from the desired. However, for the larger spot sizes, the model struggles with estimating $\Delta\phi$ values close to π for

small Xs. This is believed to result from the abundance of information at the center of the image due to the individual bifurcation peaks becoming wider spatially. The model seems to be confusing the pixels towards the center of the image as features it is already trained to look for, resulting in inaccurate estimations. Additionally, there is more error in estimation around $|\Delta\phi/\pi| = \pm 0, 2$. However, estimations improve with larger Xs as the bifurcation peaks move closer to the center, as shown in Figs. 2d and 2e. This fact seems to suggest that the model recognizes the relative distances between the two peaks as one of the important features for estimating $|\Delta\phi|$. Future work will include addressing the issue of versatility by introducing differences in spot sizes into the training. However, the model does show potential in accurate estimations when spot sizes are roughly within 10% of each other.



(a) 70% nominal (b) 80% nominal (c) 90% nominal

(d) 110% nominal (e) 120% nominal (f) 130% nominal

Figure 8: Input $\Delta\phi/\pi$ vs Model Returned $\Delta\phi/\pi$ for varying spot sizes.

3.2 EXPERIMENTAL RESULTS

This section explores the utility of employing the previously trained CNN model on experimentally collected data. It should be noted again that this data is not collected in the presence of a shock wave, but rather an optical-phase discontinuity imposed by a spatial light modulator (SLM). As mentioned previously, the goal is to build a robust, shock-tolerant reconstruction algorithm. As a first step, we modeled the shock wave as a phase discontinuity in both simulation and experiment.

To collect data, an SLM was used to impart phase discontinuities onto laser light which was then reimaged onto an SHWFS. The experimental setup and method of collecting data are outlined in Ref. 18. Here, the phase discontinuity occurred at Xs = 0 and ranged from $\Delta\phi = 0$ to 2π radians in increments of 0.05π radians. Due to the nonuniform illumination of the SHWFS sub-apertures caused by the use of a Gaussian beam, only the center-most SHWFS sub-apertures were extracted from each image. Furthermore, the use of the SLM to impart phase discontinuities adds additional diffraction to each irradiance pattern. To address this, each extracted irradiance image was normalized by the maximum, single-pixel value and then squared to ensure each image contained distinct patterns.

The same model trained in Sec. 3.1, was tested using the experimentally collected SLM-SHWFS data. Testing of this data showed a mean absolute error of 0.909 radians. Figure 9 shows the input versus model returned

$|\Delta\phi/\pi|$ for the SLM-SHWFS, single-aperture test data. Here it is shown that the model accurately estimates $|\Delta\phi/\pi|$ for input values greater than 0.25. For $|\Delta\phi/\pi| < 0.25$, the resulting irradiance pattern does not exhibit enough spreading for the model to distinguish it from an unperturbed irradiance pattern. Figure 10 shows the one-dimensional slice through the center of a single SHWFS sub-aperture irradiance pattern for 0.20π (left) and π (right) radian discontinuities. It can be seen that for the 0.20π radian discontinuity case, there is no distinct second peak from bifurcation but rather a secondary peak from *normal* diffraction through a square aperture, resulting to inaccurate estimations which leads to the high mean absolute error of 0.909 radians. This inaccuracy does not pose a problem in the scope of continuous OPD reconstruction because, as shown in Ref. 9, the traditional approach using SHWFS data in combination with a least-squares reconstruction algorithm yields accurate results for a shock-induced $\Delta\phi/\pi < 0.5$. Irradiance patterns with associated discontinuities below 0.5π will not be recognized by the current shock-tolerant reconstruction algorithm and therefore will be passed to traditional reconstruction. Furthermore, the inaccuracy shown here is a result of experimentation error, not model error. With that in mind, it can be stated with confidence that a CNN model trained in the fashion outlined in Sec. 3.1 yields accurate estimates of $\Delta\phi/\pi$ from experimentally collected irradiance pattern imagery alone.

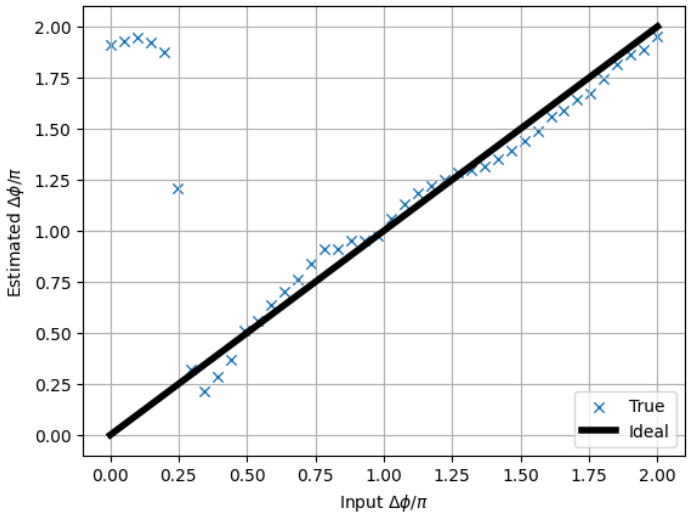
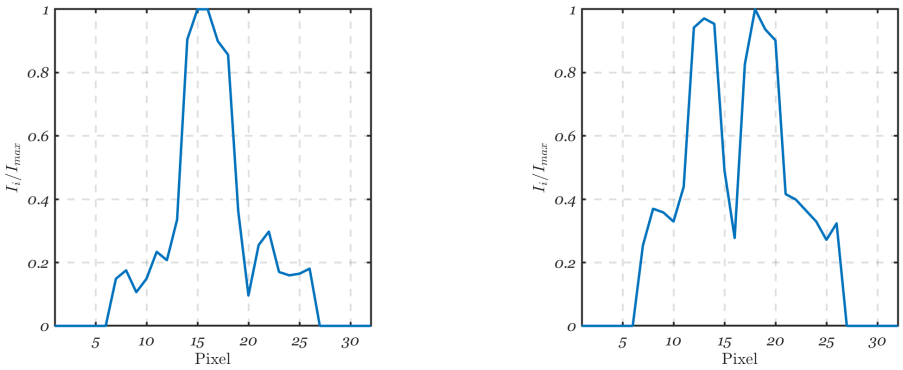


Figure 9: Input $\Delta\phi/\pi$ vs Model Returned $\Delta\phi/\pi$ for experimentally collected SHWFS imagery.



(a) $\Delta\phi = 0.20\pi$ (b) $\Delta\phi = \pi$

Figure 10: One-dimensional slices through the center of a single experimentally collected SHWFS sub-aperture.

4. CONCLUSION

This paper explored the efficacy of employing machine learning to estimate the strength of optical-phase discontinuities from far-field irradiance patterns using both simulated and experimental data. An encoder-style CNN was developed to receive 32×32×1 irradiance pattern images and return the estimated $\Delta\phi$ which caused the aberration present within the image. The model was first trained and validated using simulated data with additive background noise of normally distributed values at 1% the maximum irradiance value and differing locations of the phase discontinuity within the aperture. The model was then tested on similar data with noise levels of 0%, 2%, and 5% maximum. Testing resulted in mean absolute errors of 0.063 radians, 0.101 radians, and 0.475 radians, respectively. There are some inaccurate estimations present around 0 and 2π, however, this does not pose any issues because any aberration present in the beam at these points will be negligible and the usual centroiding algorithm would be used for those points for OPD field reconstruction purposes.

Next, the very same model's versatility was determined by testing on irradiance imagery with varying spot sizes. For smaller spot sizes cases, the model performed close to the nominal but with more error around $|\Delta\phi/\pi| = 0, 2$. However, for larger spot sizes, the model began to mistake new information toward the center of each image for the cases close to $|\Delta\phi/\pi| = 1$ as patterns it has been trained to recognize. This did improve, however, as the discontinuity approaches the aperture border where the irradiance peaks move closer together, suggesting that the relative distance between the peaks is an important feature built into the model. Future training iterations will look to improve this model's versatility. However, for the present case, the model performs well with spot sizes within 10% of the nominal. Finally, the model was then tested on experimentally collected, SLM-SHWFS data. Testing of this data resulted in a mean absolute error of 0.909 radians. At $|\Delta\phi| < 0.25\pi$ radians, the resulting irradiance imagery does not bifurcate due to the nature of the experiment. However, at all other values, the model yields accurate estimations.

The use of an encoder-style CNN to estimate associated optical-phase discontinuity from far-field irradiance patterns proves accurate in simulation and experiment, with the exception of testing performed on spot sizes that significantly differed beyond what the model was trained on. Implementing machine learning into the current shock-tolerant phase reconstruction algorithm outlined in Ref. 18 shows tremendous potential to extending the utility of the SHWFS for wavefront sensing in environments where shock waves are present.

ACKNOWLEDGMENTS

Distribution Statement A. Approved for public release: distribution is unlimited. Public Affairs release approval #: NSWCDD-PN-24-00215

REFERENCES

[1] Gordeyev, S. and Jumper, E., "Fluid dynamics and aero-optics of turrets," *Progress in Aerospace Sciences* **46**, 388–400 (nov 2010).

[2] De Lucca, N., Gordeyev, S., and Jumper, E., "In-flight aero-optics of turrets," *Optical Engineering* **52**, 071405 (jan 2013).

[3] Gordeyev, S., Jumper, E. J., and Whiteley, M., [*Aero-Optical Effects: Physics, Analysis and Mitigation*], Wiley (2023).

[4] Whiteley, M. R. and Goorskey, D. J., "Imaging performance with turret aero-optical wavefront disturbances," *Optical Engineering* **52**, 071410 (feb 2013).

[5] Kalensky, M., Catron, B., Gordeyev, S. V., Jumper, E. J., and Kemnetz, M., "Investigation of aero-mechanical jitter on a hemispherical turret," in [*Proceedings of SPIE*], Dolne, J. J. and Spencer, M. F., eds., SPIE (aug 2021).

[6] Bukowski, T. J., Gordeyev, S., Kalensky, M., and Kemnetz, M. R., "Study of unsteady surface flowfields on and around turrets with different protrusions," *AIAA Journal* **61**(12), 5320–5331 (2023).

[7] Morrida, J., Gordeyev, S., Lucca, N. D., and Jumper, E. J., "Shock-related effects on aero-optical environment for hemisphere-on-cylinder turrets at transonic speeds," *Applied Optics* **56**, 4814 (may 2017).

[8] Panda, J. and Adamovsky, G., "Laser light scattering by shock waves," *Physics of Fluids* **7**, 2271–2279 (sep 1995).

[9] Kalensky, M., Kemnetz, M. R., and Spencer, M. F., "Effects of shock waves on shack–hartmann wavefront sensor data," *AIAA Journal* , 1–13 (mar 2023).

[10] Kalensky, M., Kemnetz, M. R., and Spencer, M. F., "Effects of shock-related discontinuities on shwfs measurements: modeling and simulation," SPIE Optics and Photonics (oct 2022).

[11] Kemnetz, M. R., Kalensky, M., DeFoor, T. E., and Spencer, M. F., "Experimental investigation into the effects of shock waves on Shack-Hartmann wavefront sensor measurements," in [*Unconventional Imaging, Sensing, and Adaptive Optics 2023*], Dolne, J. J., Spencer, M. F., and Bose-Pillai, S. R., eds., **12693**, 1269314, International Society for Optics and Photonics, SPIE (2023).

[12] Chu, E. D., Bukowski, T. J., and Gordeyev, S., "Studies of local shock effects on Shack-Hartmann and digital holography wavefront sensors," in [*Unconventional Imaging, Sensing, and Adaptive Optics 2023*], Dolne, J. J., Spencer, M. F., and Bose-Pillai, S. R., eds., **12693**, 1269317, International Society for Optics and Photonics, SPIE (2023).

[13] Fried, D., "Least-square fitting a wave-front distortion estimate to an array of phase-difference measurements," *J. Opt. Soc. Am.* **67**, 370–375 (1977).

[14] Hudgin, R., "Wave-front reconstruction for compensated imaging," *J. Opt. Soc. Am.* **67**, 375–378 (1977).

[15] Southwell, W., "Wave-front estimation from wave-front slope measurements," *J. Opt. Soc. Am.* **70**(8), 998–1006 (1980).

[16] Tyson, R. K. and Frazier, B., [*Principles of Adaptive Optics: Chapter 5: Wavefront Sensing*], CRC Press (2022).

[17] Noel, Z. A., Kemnetz, M. R., Gordeyev, S., and Rennie, R. M., "Robust, regularized wavefront reconstruction of Shack-Hartmann data in discontinuous flow," in [*Unconventional Imaging, Sensing, and Adaptive Optics 2023*], Dolne, J. J., Spencer, M. F., and Bose-Pillai, S. R., eds., **12693**, 1269318, International Society for Optics and Photonics, SPIE (2023).

[18] DeFoor, T. E., Kalensky, M., Kemnetz, M. R., Bukowski, T. J., and Spencer, M. F., "Shock-wave tolerant phase reconstruction algorithm for Shack–Hartmann wavefront sensor data," *Optical Engineering* **62**(12), 123103 (2023).

[19] Suárez Gómez, S. L., González-Gutiérrez, C., Díez Alonso, E., Santos Rodríguez, J. D., Sánchez Rodríguez, M. L., Carballido Landeira, J., Basden, A., and Osborn, J., "Improving adaptive optics reconstructions with a deep learning approach," in [*Hybrid Artificial Intelligent Systems*], de Cos Juez, F. J., Villar, J. R., de la Cal, E. A., Herrero, Á., Quintián, H., Sáez, J. A., and Corchado, E., eds., 74–83, Springer International Publishing, Cham (2018).

[20] Swanson, R., Lamb, M., Correia, C., Sivanandam, S., and Kutulakos, K., "Wavefront reconstruction and prediction with convolutional neural networks," in [*Adaptive Optics Systems VI*], Close, L. M., Schreiber, L., and Schmidt, D., eds., **10703**, 107031F, International Society for Optics and Photonics, SPIE (2018).

[21] Gu, H., Zhao, Z., Zhang, Z., Cao, S., Wu, J., and Hu, L., "High-precision wavefront reconstruction from shack-hartmann wavefront sensor data by a deep convolutional neural network," *Measurement Science and Technology* **32**, 085101 (May 2021).

[22] Noel, Z. A., Bukowski, T. J., Gordeyev, S., and Rennie, R. M., "Shack-Hartmann wavefront reconstruction by deep learning neural network for adaptive optics," in [*Unconventional Imaging, Sensing, and Adaptive Optics 2023*], Dolne, J. J., Spencer, M. F., and Bose-Pillai, S. R., eds., **12693**, 126930G, International Society for Optics and Photonics, SPIE (2023).

[23] Sahba, S., Wilcox, C. C., McDaniel, A., Shaffer, B. D., Brunton, S. L., and Kutz, J. N., "Wavefront sensor fusion via shallow decoder neural networks for aero-optical predictive control," in [*Interferometry XXI*], North-Morris, M. B., Creath, K., and Porras-Aguilar, R., eds., **12223**, 1222303, International Society for Optics and Photonics, SPIE (2022).

[24] Sahba, S., *Machine Learning for Aero-Optical Wavefront Characterization and Forecasting*, PhD thesis, University of Washington (2023).

[25] Shaffer, B. D., Vorenberg, J. R., Wilcox, C. C., and McDaniel, A. J., "Generalizable turbulent flow forecasting for adaptive optics control," *Appl. Opt.* **62**, G1–G11 (Aug 2023).

[26] O'Shea, K. and Nash, R., "An introduction to convolutional neural networks," (2015).

[27] Géron, A., [*Hands-On Machine Learning with Scikit-Learn, Keras, and TensorFlow*], O'Reilley Media, INC. (2019).
[28] Aghdam, H. H., Heravi, E. J., et al., "Guide to convolutional neural networks," *New York, NY: Springer* **10**(978-973), 51 (2017).
[29] Lin, G. and Shen, W., "Research on convolutional neural network based on improved relu piecewise activation function," *Procedia Computer Science* **131**, 977–984 (2018). Recent Advancement in Information and Communication Technology:.
[30] Kingma, D. P. and Ba, J., "Adam: A method for stochastic optimization," (2017).
[31] Kalensky, M., Spencer, M. F., Jumper, E. J., and Gordeyev, S., "Estimation of atmospheric optical turbulence strength in realistic airborne environments," *Applied Optics* **61**, 6268 (July 2022).
[32] Goodman, J., [*Introduction to Fourier optics*], Roberts & Co, Englewood, Colo (2005).